nature physics

ARTICLES

https://doi.org/10.1038/s41567-021-01163-w

Optical polarization analogue in free electron beams

Hugo Lourenço-Martins[1], Davy Gérard[2] and Mathieu Kociak[3]✉

Spectromicroscopy techniques with fast electrons can quantitatively measure the optical response of excitations with unrivalled spatial resolution. However, owing to their inherently scalar nature, electron waves cannot access the polarization-related quantities. Despite promising attempts based on the conversion of concepts originating from singular optics (such as vortex beams), the definition of an optical polarization analogue for fast electrons has remained an open question. Here we establish such an analogue using the dipole transition vector of the electron between two well-chosen singular wave states. We show that electron energy loss spectroscopy allows the direct measurement of the polarized electromagnetic local density of states. In particular, in the case of circular polarization, it directly measures the local optical spin density. This work establishes electron energy loss spectroscopy as a quantitative technique to tackle fundamental issues in nano-optics, such as super-chirality, local polarization of dark excitations or polarization singularities at the nanoscale.

Classical wave optics and quantum mechanics share strong similarities rooted in the underlying Helmholtz or Schrödinger equations[1]. This very close resemblance is, for example, directly translated in the great amount of optical–electronic analogue phenomena, from the much celebrated Young–Feynman double-slit experiment[2,3] to more exotic yet fascinating examples such as corrals[4,5] or Anderson localization[6,7].

This mesmerizing analogy initiated a long-standing and fruitful dialogue between these two fields. A famous example is the development of transmission electron microscopy, strongly inspired by optical concepts[8–10]. Conversely, electron microscopy also influenced its photonic counterpart through the discovery of holography[11]. This mutual influence culminated a decade ago when electron vortices were predicted[12] and measured[13–15]—these exotic beams constituting a canonical example of a generic wave phenomenon[16] first observed with light[17].

This analogy was more recently extended to the inelastic interaction of light or electrons with matter; an example is provided in ref. [18]. In particular, electron energy loss spectroscopy (EELS) and light extinction spectroscopy (LES) give extremely similar results when interacting with optical media[19]. Also, the spatial and spectral variations in the electron energy loss intensity can be described using the nano-optical concept of electromagnetic local density of states (EMLDOS)[20] and therefore gives access to bright as well as dark modes[19–22]. Nevertheless, EELS in an electron microscope is seriously hindered by its well-known inability to measure the polarization of photonic excitations, which is rooted in the scalar character of the Schrödinger equation. Now, the importance of polarization effects at the nanoscale is not to be demonstrated, and developing polarized EELS (pEELS) could potentially shine light on the sometimes controversial[23] nanoscale polarization effects such as super-chirality[24–26], namely, the local enhancement in circular dichroism beyond what is possible with a circularly polarized plane wave.

Recent advances have shown the potential of phase-shaped free electron beams to reproduce optical polarization in EELS experiments. Indeed, the visionary work of Asenjo-Garcia and García de Abajo pointed to the use of vortex beams to mimic circular polarization[27]. Later, Guzzinati et al.[28] used π beams—singular electron beams with a π-phase jump in the plane perpendicular to the electron propagation direction—to emulate an optical-polarization-dependent experiment in EELS. Although it is based on different physical assumptions[29], the selection-rule-based approach developed in these works is essentially similar to that developed for describing dichroic signals in the so-called core-loss EELS[30]. All together, these pioneering works, as well as the phenomenological work of Ugarte and Ducati[31] and the numerical investigation of Zanfrognini and collaborators[32], gave important hints on the relation between the symmetry of free electron beams and optical polarization. Unfortunately, they did not relate the EELS probabilities to any universal macroscopic or nanoscopic optical quantity. Additionally, it remained unclear what physical vectorial quantity for free electrons shall be used as an analogue to optical polarization.

In this Article, we rigorously define an optical polarization analogue (OPA) for fast electrons as a vector equal to the transition dipole between two phase-shaped states. We then investigate the case where the beam waist of the electron beam, w_0, is larger or comparable to the typical variation length of the probed nano-optical field L. Further, we demonstrate that the polarized EELS and the linear/circular optical extinction cross-sections can be directly connected, provided that the incoming and outgoing electron states are properly defined. Particularly, we show the perfect analogy of the role of linear polarization dephasing upon wave propagation in the observation of circular dichroism in pEELS and LES. In the case of nanoscale electron beams ($w_0 \ll L$), we show that pEELS measures the EMLDOS polarized linearly or circularly in the direction perpendicular to the electron propagation axis. This result sharply contrasts with conventional EELS experiments that only access the component of the EMLDOS oriented along the beam propagation axis. Additionally, we demonstrate that the circular dichroism in pEELS is proportional to the local density of the spin of the nano-optical field.

[1]University of Göttingen, IV. Physical Institute, Göttingen, Germany. [2]Light, nanomaterials & nanotechnologies (L2n), CNRS-ERL 7004, Université de Technologie de Troyes, Troyes, France. [3]Université Paris-Saclay, CNRS, Laboratoire de Physique des Solides, Orsay, France. ✉e-mail: mathieu.kociak@universite-paris-saclay.fr

In the following, all the calculations make use of the quasi-static approximation for which we introduce the electrostatic potential propagator $W(\mathbf{r},\mathbf{r}',\omega)$ at points $\mathbf{r}$ and $\mathbf{r}'$ and angular frequency ω. We use a modal decomposition[33,34] for performing simulations within the boundary element method[35]; Supplementary Section 10 provides the relevant details. We describe the fast electron beam within the paraxial and non-recoil approximations[36] where the wavefunction is $\psi(\mathbf{r}) \propto \Psi(\mathbf{R})e^{iK_z z}$, K_z is the wavevector of the electron along its propagation axis z and $\mathbf{r}=(\mathbf{R},z)$. Therefore, the EELS probability related to a transition from the initial electron states $\psi_i(\mathbf{r})$ and final electron states $\psi_f(\mathbf{r})$ with an energy loss $\hbar\omega$ can be expressed as[27,28,32,36]

$$\Gamma_{i,f}(\omega) = \frac{2e^2}{h v^2}\iint d\mathbf{r}\, d\mathbf{r}'\ \mathrm{Im}\{-W(\mathbf{r},\mathbf{r}',\omega)\} \times \Psi_f^*(\mathbf{R})\Psi_i(\mathbf{R})\Psi_f(\mathbf{R}')\Psi_i^*(\mathbf{R}')e^{-iq_z(z-z')} \quad (1)$$

where h is the Planck constant; $q_z = K_{zf} - K_{zi} = \omega/v$ is the longitudinal momentum transfer; K_{zf} and K_{zi} denote the initial and final longitudinal momentum of the electron, respectively; further, $v \approx c/2$ is the electron speed in the transmission electron microscope, where c is the speed of light in a vacuum.

We compare the LES and pEELS techniques in Fig. 1. Evidently, pEELS requires measuring the transitions between the specific states to happen, as shown in Fig. 1a–d. Although transitions between arbitrary states are possible (also see Extended Data Fig. 1), we will consider—without loss of generality—that the incident beam Ψ_i is supposed to be an idealized vortex beam, that is, a Laguerre–Gauss $(\mathrm{LG}_{\pm 1,0)})$ (ref. [37]) or a π beam (Hermite–Gauss state $\mathrm{HG}_{0|1,1|0}$) (ref. [28]). Figure 1e shows the Poincaré sphere that describes all the possible polarization vectors $\mathbf{u}$ of light, from linear ($\mathbf{u}=\mathbf{u}_{x|y}$) to right-handed (R) or left-handed (L) circular polarization ($\mathbf{u}_{R/L}=\mathbf{u}_x \mp i\mathbf{u}_y$). As shown in Fig. 1f, a similar representation exists with the Bloch spheres for the electron states, for example $\mathrm{LG}_{1,0}=(\mathrm{HG}_{0,1}-i\mathrm{HG}_{1,0})/\sqrt{2}$.

If the realization of an LES experiment is well known (Fig. 1g), the pEELS one is worth discussing (Fig. 1h). The initial states are typically created with holographic[14,15], magnetic[28] or programmable[38] phase plates. The final state Ψ_f should be assumed to be an $\mathrm{LG}_{0,0}$ (or equivalently an $\mathrm{HG}_{0,0}$) state. Sorting such final states would require a state sorter (Fig. 1h), which is still a subject of intense experimental research[39,40]. Therefore, the preferred realization is a very small spectrometer entrance aperture, that is, a plane wave Ψ_0 as the final state, which, however, shares the same symmetry with the $\mathrm{LG}_{0,0}$ and $\mathrm{HG}_{0,0}$ states. Using a plane wave as the final state trades off the signal-to-noise ratio with ease of use[28]. The typical entrance angle range must be smaller than the ratio between the energy loss (few electron volts) to the electron acceleration voltage (~100 kV), of the order of tens of microradians (see the quantitative evaluations provided in Supplementary Section 9); the case of metallic nanoantenna is shown in Extended Data Fig. 2.

To understand the relation between optical and electron polarizations, one first needs to answer the question 'how a scalar field (electron wavefunction) can measure and project a vectorial quantity (electromagnetic field) along specific directions'?

For an LES experiment (Fig. 1g), the polarization effect directly follows from the fact that an external electromagnetic vectorial field, for example, an electrical field $\mathbf{E}_\mathbf{u}$ ($\mathbf{u}$ is either x/y or R/L), interacts with another vectorial field, that is, the polarization density in the medium. In the electronic case, it seems really tempting to naively attribute the role of the external field to the transverse wavefunction Ψ. However, when drawing the analogy between the optical and electronic cases, we must keep in mind a fundamental difference. In optical experiments, the probing wave (light) is directly involved in the process, while in electronic experiments, it is inelastically scattered via the exchange of a photon. Therefore, in the latter case, the

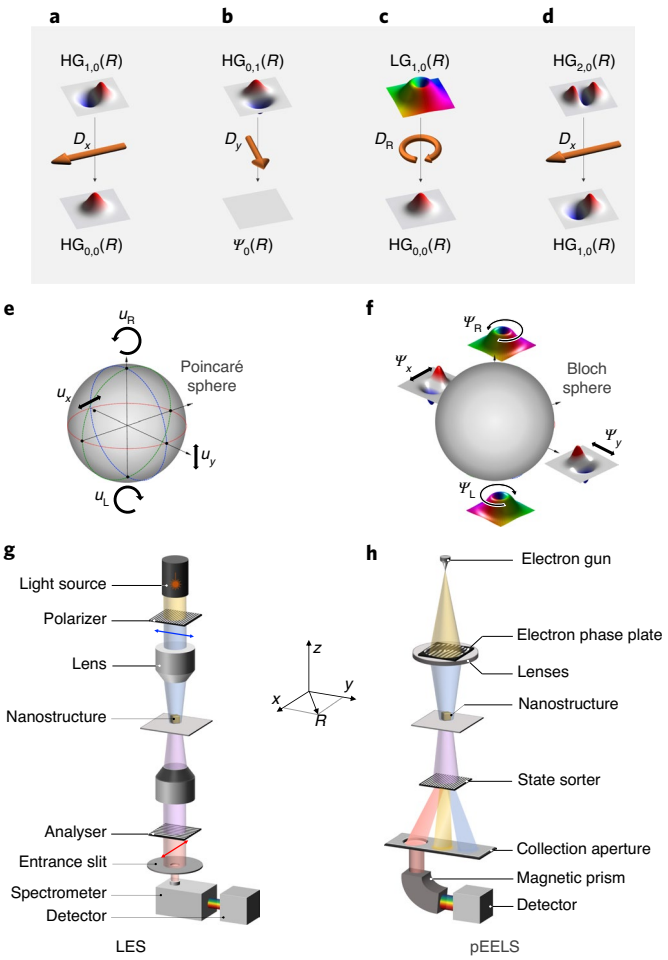

Fig. 1 | Comparison of polarized LES and polarized EELS. a–d, Examples of four different transitions carrying a non-zero transition dipole moment. This includes transition from low-order HG (**a**,**b**) or LG (**c**) states to constant-phase states (zero-order HG or LG, or plane waves) or transitions between higher-order states (**d**). **e**,**f**, Relation between linear and circular polarizations ($\mathrm{HG}_{0|1,1|0}$ and $\mathrm{LG}_{\pm 1,0}$) wavefunctions, respectively) is shown in **e** and the Poincaré sphere (Bloch sphere) is shown in **f**. **g**,**h**, Experimental setups of LES (**g**) and pEELS (**h**).

symmetry of the transition—and not of the wave itself—has to be taken into account[27,28]. To quantitatively understand this point, we start by introducing the in-plane transition dipole $\mathbf{d}_{i,f} = \langle\Psi_f|\hat{\mathbf{d}}|\Psi_i\rangle$ between an initial and final state, where $\hat{\mathbf{d}}$ denotes the transverse transition dipole moment operator for the fast electron. Without any loss of generality, we then calculate it between any first-order Hermite–Laguerre–Gaussian (HLG) state of the Bloch sphere Ψ (Fig. 1f) to the plane wave Ψ_0. The orthogonality relations of the HLG states gives (Supplementary Section 6.3)

$$\langle\Psi_0|\hat{\mathbf{d}}|\Psi\rangle = e w_0\sqrt{2\pi}\mathbf{u}, \quad (2)$$

where w_0 denotes the width of the electron beam and $\mathbf{u}$ denotes a unit vector (its relevance is discussed later). We now define the spatially dependent OPA of direction $\mathbf{u}$ as

$$\mathcal{D}_\mathbf{u}(\mathbf{R}) = \langle\Psi_0|\hat{\mathbf{d}}|\Psi\rangle f_{\mathbf{R}_0,w_0}(\mathbf{R}) \quad (3)$$

where $f_{\mathbf{R}_0,w_0}(\mathbf{R}) = \exp((\mathbf{R}-\mathbf{R}_0)^2/w_0^2)/\pi w_0^2$ is a Gaussian beam profile of width w_0 and centre $\mathbf{R}_0$, the latter corresponding to the impact parameter of the electron beam. Finally, we introduce an effective transition current as

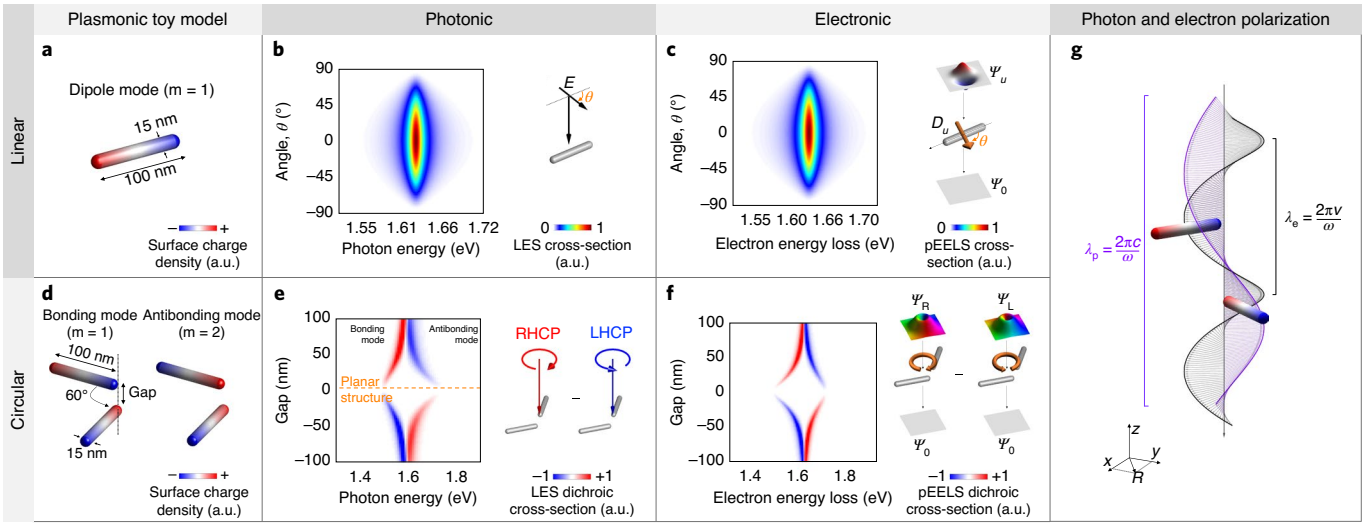

Fig. 2 | Comparison of linearly and circularly polarized LES and non-spatially resolved pEELS experiments on simple plasmonic nanostructures. a, Silver antenna sustaining a dipolar plasmon mode. **b**,**c**, Malus' law measured on the antenna with light (**b**, LES) and electronic (**c**, pEELS) excitations. In this case, the electron beam is centred in the middle of the antenna. **d**, The simplest three-dimensional optically active plasmonic structure is built by combining two antennas similar to the one shown in **a**. These two antennas form an angle of 60° and are offset along *z* by a variable distance denoted as the gap. **e**,**f**, The activity increases with a decreasing gap, similar to optical (**e**) and electronic (**f**) measurements. R(L)HCP: Right-(left-)handed circular polarization. In this case, the electron beam is centred on the tips of the two antennas. **g**, Schematic showing the propagation of a plane wave of wavelength λ_p (purple line) and an effective electron transition current of wavelength λ_e (black line) along a BKS nanostructure.

$$\mathbf{j}_{\mathbf{u}}(\mathbf{r}) = \mathcal{D}_{\mathbf{u}}(\mathbf{R})\ \mathrm{e}^{iq_z z}. \tag{4}$$

It should be noted that this current has the form of an optical plane wave, where the wave vector $q_z = \omega/v$ is the transferred momentum.

To get the EELS probability from equation (1), we apply the generic relations of the Hermite–Gauss functions (Supplementary Section 12) to the first-order HG states $\mathrm{HG}_{0|1,1|0}$. We show that for any function $g(\mathbf{R})$, $\int g(\mathbf{R})\mathrm{HG}_{1,0}(\mathbf{R}) \propto \int \partial_x g(\mathbf{R}) f_{\mathbf{R}_0,w_0}(\mathbf{R})$, while the $\mathrm{HG}_{0|1}$ state gives a derivative along the *y* axis. We then introduce the electric field propagator $\mathbf{G}(\mathbf{r},\mathbf{r}',\omega)$ related to $W(\mathbf{r},\mathbf{r}',\omega)$ through $4\pi\omega^2\mathbf{G}(\mathbf{r},\mathbf{r}',\omega) = \nabla\nabla' W(\mathbf{r},\mathbf{r}',\omega)$. This permits to integrate by parts equation (1); further, by using the previous equations, we find the transition probability from any first-order HLG state to Ψ_0 as

$$\Gamma_{\mathbf{u}}(\mathbf{R}_0,\omega) = \tfrac{4q_z^2}{\hbar}\iint \mathrm{d}\mathbf{r}\ \mathrm{d}\mathbf{r}'\ \ \mathrm{Im}\left\{-\mathbf{j}_{\mathbf{u}}(\mathbf{r}).\overleftrightarrow{\mathbf{G}}(\mathbf{r},\mathbf{r}',\omega).\mathbf{j}_{\mathbf{u}}(\mathbf{r}')\right\} \tag{5}$$

Equation (5) is now a scalar product similarly to the optical case. Further, $\mathcal{D}_u$ is an in-plane transition dipole moment that defines a polarization analogue for EELS, with $\mathbf{u} = \mathbf{d}_{i,f}/|\mathbf{d}_{i,f}|$ is the direction of the in-plane transition dipole $\mathbf{d}_{if}$. Remarkably, in the case of a transition between $|\Psi\rangle$ to $|\Psi_0\rangle$, $\mathbf{u}$ corresponds to the point of the Poincaré sphere (Fig. 1e) located at the same coordinate as Ψ on the Bloch sphere, giving an intuitive mapping between both spheres. However, more generally, the transition between the initial and final state gives rise to the vectorial form of the electron polarization analogue. Therefore, for arbitrary transitions between $\mathrm{HG}_{n,m}$ and $\mathrm{HG}_{n',m'}$ states, a less intuitive mapping should be made by respecting the selection rules $n' = n \pm 1$ or $m' = m \pm 1$ (linear case) or with $\mathrm{LG}_{l,m}$ and $\mathrm{LG}_{l',m}$ $l' = l \pm 1$ (circular case) (Supplementary Section 8 and Extended Data Fig. 1), that is, in cases where the phase structure of the initial and final states has no obvious dipolar symmetry. We note that—within the non-recoil approximation—we have not made any assumption on the specific energy transferred to the target; therefore, the above description is perfectly valid for probing any solid-state excitations, from phonons to core-loss excitation.

In the following, we will determine the optical observables measured with pEELS. We first consider the broad illumination limit ($w_0 \gtrsim L$) in which light and electron beams can be compared, as shown in Fig. 1. The extinction cross-section for a plane wave polarized along the direction $\mathbf{u}$ has a well-known proportionality relation with the polarizability tensor $\boldsymbol{\alpha}$ (Fig. 1g and Supplementary Section 4):

$$\sigma_{\mathbf{u}}(\omega) = 4\pi k_z^2 \iint \mathrm{d}\mathbf{R}\ \mathrm{d}\mathbf{R}'\ \ \mathrm{Im}\left\{\alpha_{\mathrm{uu}}(\mathbf{R},\mathbf{R}',\mathrm{k}_z,-\mathrm{k}_z,\omega)\right\} \tag{6}$$

where $k_z = \omega/c$ is the wavevector of the electromagnetic plane wave propagating along *z*. This has to be compared with the electronic case, where the normalized pEELS probability $\overline{\Gamma}_{\mathbf{u}} = \frac{\Gamma_{\mathbf{u}}}{2\pi w_0^2}$ for a transition dipole $\mathcal{D}_u$ can be deduced from equation (5) by noting that the integrations along *z* and *z*′ correspond to two time-domain Fourier transforms (FTs) and reads

$$\begin{aligned}\overline{\Gamma}_{\mathbf{u}}(\mathbf{R}_0,\omega) = {} & \tfrac{4e^2}{\hbar} q_z^2 \iint \mathrm{d}\mathbf{R}\ \mathrm{d}\mathbf{R}'\, f_{\mathbf{R}_0,w_0}(\mathbf{R})\, f_{\mathbf{R}_0,w_0}(\mathbf{R}') \\ & \mathrm{Im}\left\{-G_{\mathbf{uu}}(\mathbf{R},\mathbf{R}',q_z,-q_z,\omega)\right\}\end{aligned} \tag{7}$$

Note that the polarizabilities and Green dyadics are simply connected through a Dyson equation[41], which reduces to a simple proportionality relation (in the sense of tensors) for a dipole in a vacuum.

The almost perfect resemblance between equations (6) and (7) shows that pEELS is the counterpart of the polarized optical extinction experiment, in the same vein as the correspondence between regular EELS and unpolarized extinction[19]. This is further exemplified for the linear polarization case (Fig. 2a–c), where the Malus' law for the dipolar mode of a silver nanoantenna is fully retrieved in both photonic and electronic cases (Fig. 2b,c), re-enforcing the analogy between the optical polarization vector and $\mathcal{D}_u$. Nevertheless, contrary to the optical case, the pEELS probability depends on the precise positioning of the beam through its dependence upon $\mathbf{R}_0$.

Further, the photonic circular dichroic extinction is interesting. Omitting the spatial and frequency dependencies for

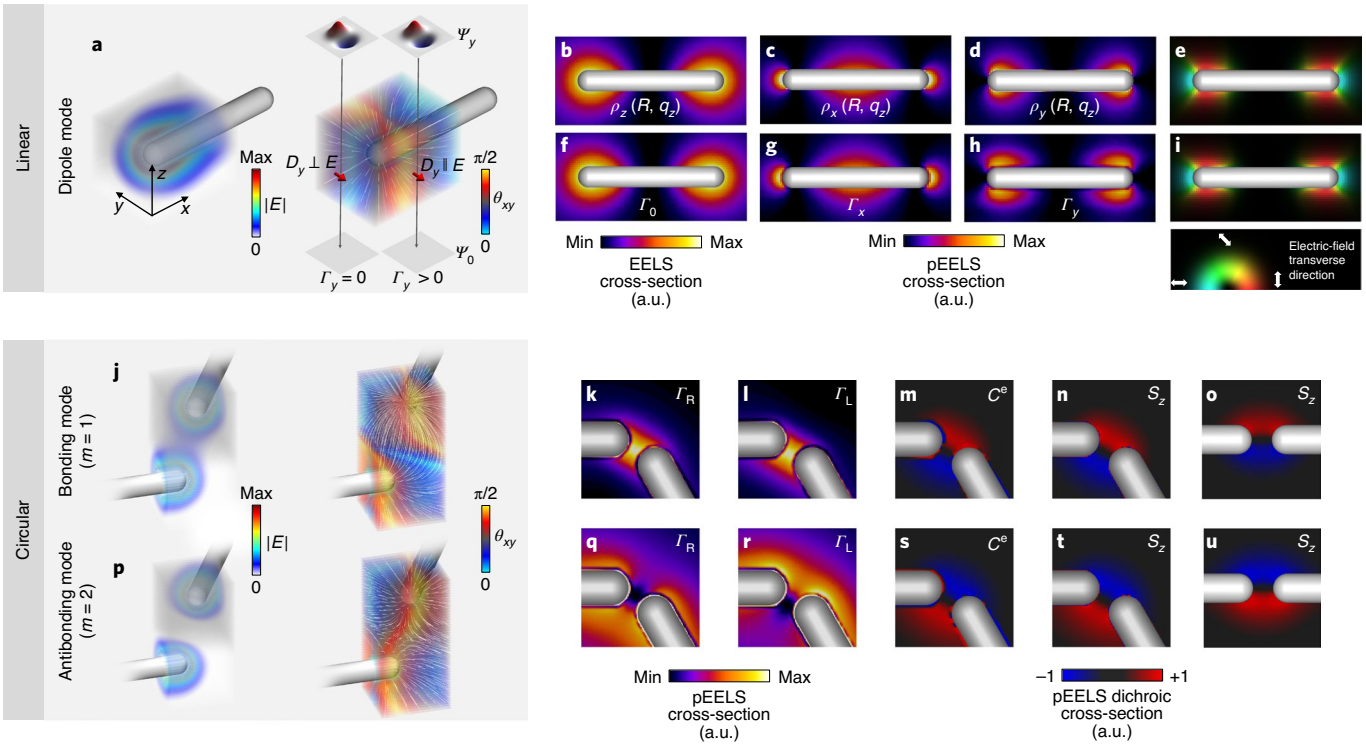

Fig. 3 | Spatially resolved pEELS. a–i, Spatially resolved linear pEELS of the dipolar mode of silver nanoantennas. **a**, Three-dimensional maps of the electric field magnitude and transverse direction θ_{xy} of the dipole mode (Fig. 2a) around one tip of the rod. The field lines are represented in white. The dipole moment $\mathcal{D}_y$ of the transition $\Psi_y \rightarrow \Psi_0$ is represented at two different positions of the electron beam. **b**–**d**, FT EMLDOS calculated along the *z* axis (**b**), *x* axis (**c**) and *y* axis (**d**). **f**–**h**, The pEELS maps simulated with the Ψ_0 (**f**), Ψ_x (**g**) and Ψ_y (**h**) wavefunctions. **e**,**i**, Electric-field transverse direction respectively reconstructed from **b**–**d** (**e**) and **f**–**h** (**f**) and plotted using a domain colouring method. **j**–**u**, Spatially resolved circular dichroic pEELS signal for the BKS shown in Fig. 2d with a fixed gap at 25 nm. **j**, Three-dimensional map of the electric field magnitude and transverse direction θ_{xy} of the bonding mode. The field lines are represented in white. **p**, Same map as **j** but for the antibonding mode. **k**,**l**, The pEELS maps of the bonding mode calculated for Ψ_R (**k**) and Ψ_L (**l**) wavefunction. **m**, Dichroic pEELS map deduced from **k** and **l**. **n**, Map of the optical-field spin density along *z* of the bonding mode. **q**–**t**, Same calculations as **k**–**n** but for the antibonding mode. **o**,**u**, Same maps as **n** (**o**) and **t** (**t**), except that the BKS structure is aligned.

brevity, it is defined by $\mathcal{C}^o = \sigma_R - \sigma_L \propto \iint d\mathbf{R}\, d\mathbf{R}'\, \mathrm{Re}\{\alpha_{yx} - \alpha_{xy}\}$ and the EELS one is defined as $\mathcal{C}^e(\mathbf{R}_0, \omega) = \Gamma_R - \Gamma_L \propto \iint d\mathbf{R}\, d\mathbf{R}'\, \mathrm{Re}\{G_{xy} - G_{yx}\} f(\mathbf{R}) f(\mathbf{R}')$ (Supplementary Section 5.2). Clearly, $\mathcal{C}^o$ and $\mathcal{C}^e$ are also analogues.

This is exemplified when comparing circularly polarized LES and EELS for the simplest chiral plasmonic structure, the so-called Born–Kuhn model system (BKS)[42]. The BKS is built from two antennas sustaining dipole resonances offset along the *z* direction and rotated with respect to each other (Fig. 2d). The gap and the angle set the effective dephasing between the two subsequent interactions between the probe and each antenna. Both optic and electronic situations are almost identical with (1) an increase in the dichroism visibility as the gap decreases and (2) an inversion of the dichroism when the sign of the gap flips—in perfect agreement with optical experiments reported in the literature[43]. The strong circular dichroic signals stem from the exact same physical ground. In both cases, the circular polarization vector can be decomposed as a sum of the linear polarization vectors. The linear polarization rotates upon propagation, exciting for the *R* polarization in phase (antiphase) with the two dipolar charge distributions of the bounding (antibounding) mode (Fig. 2g). The only difference is the rotation speed of the linear polarization, which is related to the light wavelength $2\pi c/\omega$ and the wavelength $2\pi v/\omega$ of the electromagnetic field following the electrons. Since the electron speed can be changed at will, this makes EELS a fairly tunable tool for the investigation of chiral structures, as already suggested for photon-induced near-field electron microscopy (PINEM)[44].

We now turn to the focused illumination limit ($w_0 \ll L$) (Fig. 3a,j,p). Using the fact that a Gaussian function of a vanishing waist tends to a Dirac distribution, we can directly re-express equation (7) (Supplementary Section 3.3 provides alternative demonstrations) and find a spatially resolved pEELS experiment between states i and f (Supplementary Section 5):

$$\Gamma_{\mathbf{u}}^{\mathrm{i,f}}(\mathbf{R}_0, \omega) = \frac{2\pi q_z^2}{\hbar\omega} \left|\mathbf{d}_{\mathrm{i,f}}\right|^2 \tilde{\rho}_{\mathbf{uu}}(\mathbf{R}_0, q_z, \omega) \tag{8}$$

where $\tilde{\rho}_{\mathbf{uu}}(\mathbf{R}_0, q_z, \omega)$ denotes the FT (along *z*) **u**-polarized EMLDOS defined as[20]

$$\rho_{\mathbf{u}}(\mathbf{r}, \omega) = -\frac{2\omega}{\pi} \mathrm{Im}\left\{\mathbf{u}^* \cdot \overleftrightarrow{\mathbf{G}}(\mathbf{r}, \mathbf{r}, \omega) \cdot \mathbf{u}\right\} \tag{9}$$

Therefore, pEELS is directly proportional to the FT along *z* of the EMLDOS polarized in a plane perpendicular to the electron beam axis, while regular EELS is related to the FT of the EMLDOS polarized along the electron beam direction[20]. We emphasize that since **u** is any polarization of the Poincaré sphere, the latter equation extends the definition of the chiral EMLDOS described by Pham et al.[45,46] Remarkably, it is evident that equation (8) is extremely similar to the decay rate enhancement of a dipole placed in an electromagnetic environment (Purcell effect[47]), with the electron-transition dipole moment playing the role of a probe dipole (Supplementary Section 6.4). Therefore, this demonstrates that the transverse free

electron state behaves analogously to a two-state system interacting with a nano-optical field, where the interaction time is encoded in the z-FT.

To illustrate our findings, we simulated a spatially resolved pEELS experiment on the dipole mode of the same antenna as shown in Fig. 2a. As shown in Fig. 3a, we computed the three-dimensional map of the magnitude $|E|$ and transverse direction $\theta_{xy} = \arctan(|E_y|/|E_x|)$ of the plasmonic electric field. As expected, one can observe that the FT z EMLDOS (Fig. 3b) clearly reproduces the variations in the field magnitude (Fig. 3a), while the FT x and y EMLDOS (Fig. 3c,d) map the regions where the field is aligned along the x and y directions, respectively, as shown in blue and yellow in Fig. 3a. This simple correspondence comes from the fact that the transverse direction of the electric field does not strongly vary as a function of z (Fig. 3a). We then simulated the pEELS maps for $\Psi_0 \rightarrow \Psi_0$ ($\mathcal{D}_u = 0$), $\Psi_x \rightarrow \Psi_0$ ($\mathcal{D}_u = \mathcal{D}_x$) and $\Psi_y \rightarrow \Psi_0$ ($\mathcal{D}_u = \mathcal{D}_y$) transitions, as shown in Fig. 2f–h, respectively. One can observe an almost perfect agreement between the polarized EMLDOS and pEELS maps, which strongly supports our theoretical conclusions[8]. This result provides a clear and rigorous interpretation of the early local mapping of dipolar plasmons with a π beam[28]. Additionally, from two different linear pEELS measurements, one can reconstruct the local polarization of the optical fields (Fig. 3e,i), as otherwise measured by Krehl et al. with differential phase-contrast imaging[48]. Our technique, thus, constitutes the ideal tool to resolve polarization singularities at the nanoscale[49,50].

Plugging equation (8) in $\mathcal{C}^{\mathrm{e}} = \Gamma_{\mathrm{R}} - \Gamma_{\mathrm{L}}$, one can also rigorously define the spatially resolved dichroic pEELS probability (Supplementary Section 5.2) as

$$\mathcal{C}^{\mathrm{e}} = \frac{2\pi e^2 q_z^2}{\hbar\omega}\left(\tilde{\rho}_{\mathrm{R}}(\mathbf{R}_0, q_z, \omega) - \tilde{\rho}_{\mathrm{L}}(\mathbf{R}_0, q_z, \omega)\right) \tag{10a}$$

$$= \frac{4e^2 q_z^2}{\hbar}\,\mathrm{Re}\left\{G_{xy}(\mathbf{R}_0, q_z, \omega) - G_{yx}(\mathbf{R}_0, q_z, \omega)\right\} \tag{10b}$$

where the dependence on $\mathbf{R}_0, \omega$ and q_z on the left-hand side has been omitted for brevity. This equation allows us to formally define the optical dichroism at the nanoscale as the measure of the local difference between the density of the right- and left-handed optical states. Additionally, in both equations (10a) and (10b), the definition of the z component of the spin operator of the electromagnetic field applied on a plane wave of frequency q_z (refs. [23,51]) can be expressed as

$$\mathcal{C}^{e}(\mathbf{R}_0, q_z, \omega) = -\frac{2\pi e^2 q_z^2}{\hbar^2\omega} S_z(\mathbf{R}_0, q_z, \omega) \tag{11}$$

The latter equation shows that $\mathcal{C}^{\mathrm{e}}$ measures the q_z component of the optical spin density along the direction of propagation of the electron beam, which is itself proportional to the optical chirality flow[52]. To clearly illustrate the physics at play in this case, we numerically investigated the nano-optical dichroism of the BKS introduced in Fig. 2d with a fixed gap of 25 nm. In Fig. 3j,p, we show the maps of the magnitude and transverse direction of the plasmonic electric fields, respectively, associated with the bonding and antibonding modes (note that to facilitate visibility, the gap has been increased to 50 nm on these plots). Crucially, and as a signature of the chiral nature of the BKS, Fig. 3j,p shows that the transverse direction of the electric field rotates as a function of z, as the iso-direction regions form helices (as indicated in blue and yellow, respectively). The local spin density $S_z(\mathbf{R}_0, q_z, \omega)$ is a direct measure of this property and quantifies the direction in which the electric fields rotates along z at $\mathbf{R}_0$ and for the spatial frequency q_z. This is shown in Fig. 3k–n in the case of the bonding mode and Fig. 3q–t for the antibonding mode. Moreover, the perfect agreement observed between the maps of $\mathcal{C}^{\mathrm{e}}$ and S_z corroborate our equations (10a), (10b) and (11).

To give a more intuitive understanding, one can apply a modal decomposition to the spin operator, that is, $\overleftrightarrow{\mathbf{G}}(\mathbf{r}, \mathbf{r}', \omega) = \sum_m g_m(\omega)\mathbf{E}_m(\mathbf{r}) \otimes \mathbf{E}_m(\mathbf{r}')$, where m is an integer indexing the optical modes of the nanostructure and g_m is the so-called spectral response function (see Supplementary Section 7 and ref. [34]). Subsequently, we get $S_z \propto \mathrm{Im}\{\mathrm{E_m} \times \mathrm{E_m^*}\}_z$, which corresponds to the Minkowski formula for the spin of optical fields[53,54]; this clearly shows its connection with the local twist of the electric field.

Finally, we can emphasize that these results shine a new light onto the microscopic origin of the extrinsic dichroism and its macroscopic expression. A nano-optical probe such as a phase-shaped electron beam measures the local difference between the right and left EMLDOS. A broad beam measures the spatially integrated difference between the left and right density of states. Consequently, a nanostructure can be optically inactive while having a non-zero density of spin (that is, the nano-optical field exhibits a local twist), as illustrated on the non-chiral aligned BKS nanostructure (Fig. 3o,u). Equation (9) can be interpreted as the Purcell effect for a chiral dipole probe (say, a molecule) placed at point $\mathbf{R}_0$ with the same transition dipole as the one of the transverse electron wavefunction. Therefore, chiral pEELS can directly probe the location of the enhanced emission of chiral molecules even in globally achiral structures.

We have shown that we can rigorously define an OPA for the free electron beam. This leads to the possibility of introducing polarized measurements in EELS. These are directly analogous to LES experiments in the case of broad beam illuminations. Spatially resolved pEELS maps are a measurement of the polarized EMLDOSs, and the dichroic circular pEELS probabilities are directly related to the density of electromagnetic spins. In particular, this permits a comprehensive description of the local polarization of both bright and dark optical excitations, while the otherwise highly successful experiments involving polarization, e.g. cathodoluminescence[55–57] or PINEM[44,58], are restricted to the bright ones. We hope that the sound definition of the observables presented here will keep motivating the longstanding and challenging experimental developments required to experimentally observe pEELS. Remarkably, through the mapping between Bloch and Poincaré spheres, our work establishes a Jones formalism for electrons. Thus, through the consideration of partial OPA, the development of a full polarimetric[56] pEELS is now at hand. This study concentrates on the quasi-static limit, where magneto-electric and spin-related[59] effects are not taken into account. Extension to the relativistic case has already been described for the circular pEELS of molecules[27], but should be continued in a similar framework as the one developed here. Also, the formalism used here could be used as the basis to describe cathodoluminescence and PINEM experiments with phase-shaped electrons.

Online content

Any methods, additional references, Nature Research reporting summaries, source data, extended data, supplementary information, acknowledgements, peer review information; details of author contributions and competing interests; and statements of data and code availability are available at https://doi.org/10.1038/s41567-021-01163-w.

Received: 11 June 2020; Accepted: 24 December 2020;
Published online: 04 March 2021

References

1. Akkermans, E. & Montanbaux, G. *Mesoscopic Physics of Electrons and Photons* (Cambridge Univ. Press, 2010); https://doi.org/10.1017/CBO9780511618833
2. Tonomura, A., Endo, J., Matsuda, T., Kawasaki, T. & Ezawa, H. Demonstration of single electron buildup of an interference pattern. *Am. J. Phys.* **57**, 117–120 (1989).
3. Bach, R., Pope, D., Liou, S.-H. & Batelaan, H. Controlled double-slit electron diffraction. *New J. Phys.* **15**, 033018 (2013).

4. Crommie, M. F., Lutz, C. P. & Eigler, D. M. Confinement of electrons to quantum corrals on a metal surface. *Science* **262**, 218–220 (1993).
5. Colas des Francs, G. et al. Optical analogy to electronic quantum corrals. *Phys. Rev. Lett.* **86**, 4950–4953 (2001).
6. Anderson, P. W. Absence of diffusion in certain random lattices. *Phys. Rev.* **109**, 1492–1505 (1958).
7. Wiersma, D. S., Bartolini, P., Lagendijk, A. D. & Righini, R. Localization of light in a disordered medium. *Nature* **390**, 671–673 (1997).
8. Rose, H. H. *Geometrical Charged-Particle Optics* (Springer Series in Optical Sciences, Springer Berlin Heidelberg, 2013).
9. Scherzer, O. The theoretical resolution limit of the electron microscope. *J. Appl. Phys.* **20**, 20–29 (1949).
10. Haider, M. et al. Electron microscopy image enhanced. *Nature* **392**, 768–769 (1998).
11. Gabor, D. A new microscopic principle. *Nature* **161**, 777–778 (1948).
12. Bliokh, K. Y., Bliokh, Y. P., Savel'ev, S. & Nori, F. Semiclassical dynamics of electron wave packet states with phase vortices. *Phys. Rev. Lett.* **99**, 190404 (2007).
13. Uchida, M. & Tonomura, A. Generation of electron beams carrying orbital angular momentum. *Nature* **464**, 737–739 (2010).
14. Verbeeck, J., Tian, H. & Schattschneider, P. Production and application of electron vortex beams. *Nature* **467**, 301–304 (2010).
15. McMorran, B. J. et al. Electron vortex beams with high quanta of orbital angular momentum. *Science* **331**, 192–195 (2011).
16. Nye, J. F. & Berry, M. V. Dislocations in wave trains. *Proc. R. Soc. A* **336**, 165–190 (1974).
17. Allen, L., Beijersbergen, M. W., Spreeuw, R. J. C. & Woerdman, J. P. Orbital angular momentum of light and the transformation of Laguerre–Gaussian laser modes. *Phys. Rev. A* **45**, 8185–8189 (1992).
18. García De Abajo, F. J., Estrada, H. & Meseguer, F. Diacritical study of light, electrons and sound scattering by particles and holes. *New J. Phys.* **11**, 1–10 (2009).
19. Losquin, A. et al. Unveiling nanometer scale extinction and scattering phenomena through combined electron energy loss spectroscopy and cathodoluminescence measurements. *Nano Lett.* **15**, 1229–1237 (2015).
20. García de Abajo, F. J. & Kociak, M. Probing the photonic local density of states with electron energy loss spectroscopy. *Phys. Rev. Lett.* **100**, 106804 (2008).
21. Nicoletti, O. et al. Three-dimensional imaging of localized surface plasmon resonances of metal nanoparticles. *Nature* **502**, 80–84 (2013).
22. Losquin, A. & Kociak, M. Link between cathodoluminescence and electron energy loss spectroscopy and the radiative and full electromagnetic local density of states. *ACS Photon.* **2**, 1619–1627 (2015).
23. Coles, M. M. & Andrews, D. L. Chirality and angular momentum in optical radiation. *Phys. Rev. A* **85**, 063810 (2012).
24. Collins, J. T. et al. Chirality and chiroptical effects in metal nanostructures: fundamentals and current trends. *Adv. Opt. Mater.* **5**, 1700182 (2017).
25. Tullius, R. et al. 'Superchiral' spectroscopy: detection of protein higher order hierarchical structure with chiral plasmonic nanostructures. *J. Am. Chem. Soc.* **137**, 8380–8383 (2015).
26. Schäferling, M., Dregely, D., Hentschel, M. & Giessen, H. Tailoring enhanced optical chirality: design principles for chiral plasmonic nanostructures. *Phys. Rev. X* **2**, 031010 (2012).
27. Asenjo-Garcia, A. & García De Abajo, F. J. Dichroism in the interaction between vortex electron beams, plasmons, and molecules. *Phys. Rev. Lett.* **113**, 1–5 (2014).
28. Guzzinati, G. et al. Probing the symmetry of the potential of localized surface plasmon resonances with phase-shaped electron beams. *Nat. Commun.* **8**, 14999 (2017).
29. Lourenço-Martins, H., Lubk, A. & Kociak, M. Bridging nano-optics and condensed matter formalisms in a unified description of inelastic scattering of relativistic electron beams. Preprint at https://arxiv.org/abs/2007.02773 (2020).
30. Schattschneider, P., Löffler, S., Stöger-Pollach, M. & Verbeeck, J. Is magnetic chiral dichroism feasible with electron vortices? *Ultramicroscopy* **136**, 81–85 (2014).
31. Ugarte, D. & Ducati, C. Controlling multipolar surface plasmon excitation through the azimuthal phase structure of electron vortex beams. *Phys. Rev. B* **93**, 1–9 (2016).
32. Zanfrognini, M. et al. Orbital angular momentum and energy loss characterization of plasmonic excitations in metallic nanostructures in TEM. *ACS Photon.* **6**, 620–627 (2019).
33. Ouyang, F. & Isaacson, M. Surface plasmon excitation of objects with arbitrary shape and dielectric constant. *Phil. Mag. B* **60**, 481–492 (1989).
34. Boudarham, G. & Kociak, M. Modal decompositions of the local electromagnetic density of states and spatially resolved electron energy loss probability in terms of geometric modes. *Phys. Rev. B* **85**, 245447 (2012).
35. Hohenester, U. Simulating electron energy loss spectroscopy with the MNPBEM toolbox. *Comput. Phys. Commun.* **185**, 1177–1187 (2014).
36. García de Abajo, F. J. Optical excitations in electron microscopy. *Rev. Mod. Phys.* **82**, 209–275 (2010).
37. Schattschneider, P., Stöger-Pollach, M. & Verbeeck, J. Novel vortex generator and mode converter for electron beams. *Phys. Rev. Lett.* **109**, 084801 (2012).
38. Verbeeck, J. et al. Demonstration of a 2×2 programmable phase plate for electrons. *Ultramicroscopy* **190**, 58–65 (2018).
39. Grillo, V. et al. Measuring the orbital angular momentum spectrum of an electron beam. *Nat. Commun.* **8**, 15536 (2017).
40. Pozzi, G. et al. Design of electrostatic phase elements for sorting the orbital angular momentum of electrons. *Ultramicroscopy* **208**, 112861 (2020).
41. Colas des Francs, G., Girard, C., Weeber, J. C. & Dereux, A. Relationship between scanning near-field optical images and local density of photonic states. *Chem. Phys. Lett.* **345**, 512–516 (2001).
42. Yin, X., Schäferling, M., Metzger, B. & Giessen, H. Interpreting chiral nanophotonic spectra: the plasmonic Born–Kuhn model. *Nano Lett.* **13**, 6238–6243 (2013).
43. Lu, X. et al. Circular dichroism from single plasmonic nanostructures with extrinsic chirality. *Nanoscale* **6**, 14244–14253 (2014).
44. Harvey, T. R. Probing chirality with inelastic electron-light scattering. *Nano Lett.* **20**, 4377–4383 (2020).
45. Pham, A. et al. Chiral optical local density of states in a spiral plasmonic cavity. *Phys. Rev. A* **94**, 053850 (2016).
46. Pham, A., Zhao, A., Genet, C. & Drezet, A. Optical chirality density and flux measured in the local density of states of spiral plasmonic structures. *Phys. Rev. A* **98**, 1–9 (2018).
47. Novotny, L. & Hecht, B. *Principles of Nano-Optics* (Cambridge Univ. Press, 2006).
48. Krehl, J. et al. Spectral field mapping in plasmonic nanostructures with nanometer resolution. *Nat. Commun.* **9**, 4207 (2018).
49. Burresi, M. et al. Observation of polarization singularities at the nanoscale. *Phys. Rev. Lett.* **102**, 033902 (2009).
50. Rotenberg, N., Feber, B., Visser, T. D. & Kuipers, L. Tracking nanoscale electric and magnetic singularities through three-dimensional space. *Optica* **2**, 540–546 (2015).
51. Kim, S. M. & Gbur, G. Angular momentum conservation in partially coherent wave fields. *Phys. Rev. A* **86**, 043814 (2012).
52. Bliokh, K. Y. & Nori, F. Characterizing optical chirality. *Phys. Rev. A* **83**, 021803 (2011).
53. Cameron, R. P., Barnett, S. M. & Yao, A. M. Optical helicity, optical spin and related quantities in electromagnetic theory. *New J. Phys.* **14**, 053050 (2012).
54. Bliokh, K. Y., Bekshaev, A. Y. & Nori, F. Dual electromagnetism: helicity, spin, momentum and angular momentum. *New J. Phys.* **15**, 033026 (2013).
55. Gómez-Medina, R., Yamamoto, N., Nakano, M. & García de Abajo, F. J. Mapping plasmons in nanoantennas via cathodoluminescence. *New J. Phys.* **10**, 105009 (2008).
56. Osorio, C. I., Coenen, T., Brenny, B. J. M., Polman, A. & Koenderink, A. F. Angle-resolved cathodoluminescence imaging polarimetry. *ACS Photon.* **3**, 147–154 (2016).
57. Polman, A., Kociak, M. & García de Abajo, F. J. Electron-beam spectroscopy for nanophotonics. *Nat. Mater.* **18**, 1158–1171 (2019).
58. Yurtsever, A. & Zewail, A. H. Direct visualization of near-fields in nanoplasmonics and nanophotonics. *Nano Lett.* **12**, 3334–3338 (2012).
59. Bliokh, K. Y. et al. Theory and applications of free-electron vortex states. *Phys. Rep.* **690**, 1–70 (2017).

Data availability

Source data are available for this paper. All other data that support the plots within this paper and other findings of this study are available from the corresponding author upon reasonable request.

Acknowledgements

We acknowledge J. Verbeeck for introduction to this field and thank J. Verbeeck, D. Ugarte, F. Houdellier and G. Guzzinati for insightful discussions. H.L.-M. thanks T. R. Harvey for insightful discussions. This project has received funding from the European Union's Horizon 2020 research and innovation programme under grant agreement no. 823717-ESTEEM3 and no. 101017720-EBEAM, from the French state managed by the National Agency for Research under the programme of future investment EQUIPEX TEMPOS-CHROMATEM with the reference ANR-10-EQPX-50 and ANR-17-CE24-0039 (2D-CHIRAL).

Author contributions

M.K. and H.L.-M. developed the theory. H.L.-M. wrote the simulation codes and performed the numerical simulations. M.K., H.L.-M. and D.G. developed the analogy between the Bloch and Poincaré spheres. All the authors discussed the results and contributed to the writing of the manuscript.

Competing interests

The authors declare no competing interests.

Additional information

Extended data is available for this paper at https://doi.org/10.1038/s41567-021-01163-w.

Supplementary information The online version contains supplementary material available at https://doi.org/10.1038/s41567-021-01163-w.

Correspondence and requests for materials should be addressed to M.K.

Peer review information *Nature Physics* thanks the anonymous reviewers for their contribution to the peer review of this work.

Reprints and permissions information is available at www.nature.com/reprints.

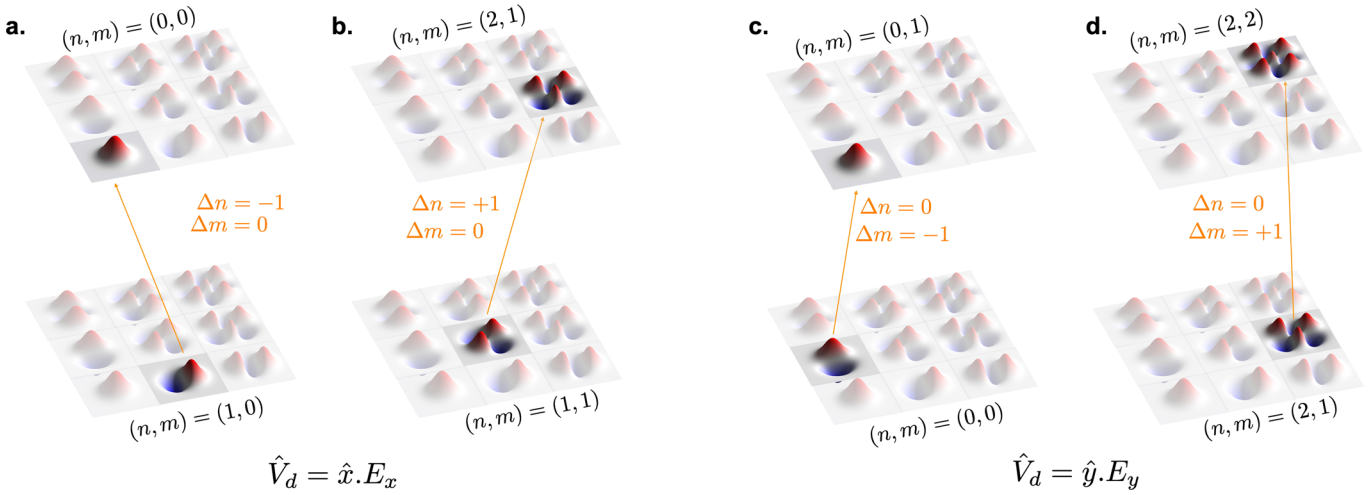

Extended Data Fig. 1 | Examples of transitions between higher order HG states possessing a non-zero OPA. Transitions **a** and **b** possess a dipole moment along the x direction and therefore measure $E_x(\omega, qz)$. Transitions **c** and **d** possess a dipole moment along the y direction and therefore measure $E_y(\omega, qz)$.

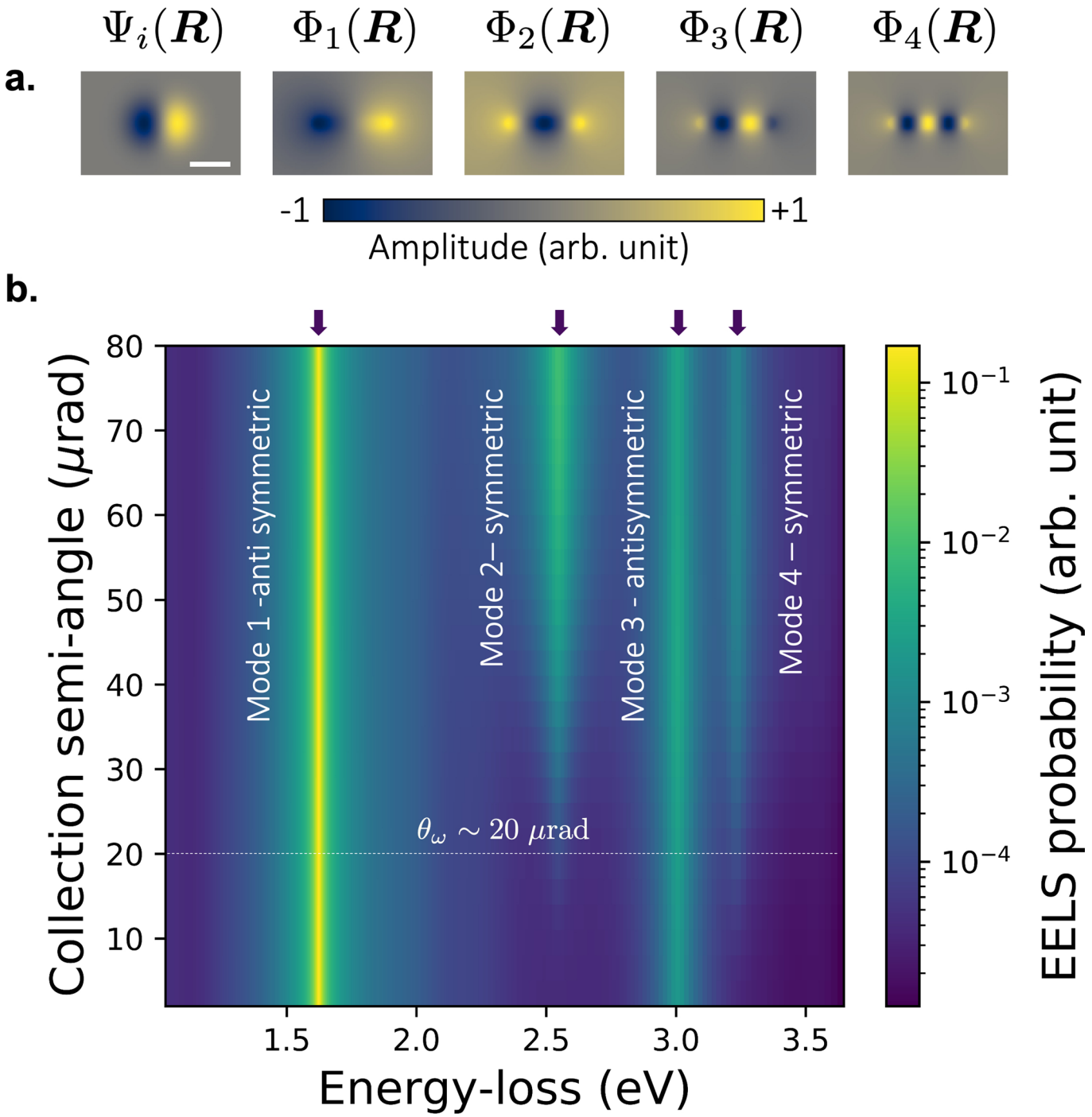

Extended Data Fig. 2 | Illustration of the effect of the summation over the final states. a, Wavefunction ψ_i and plasmonic potential ϕ_m of the four first modes m of a 100nm * 15nm silver nano-antenna. The relative position and scale of the wavefunction and potential are respected. Scales bar is 50 nm. **b**, pEELS spectrum as a function of the collection angle. The peaks of the four modes shown in a. are marked with arrows. Below θ_ω, the second and fourth peak are suppressed due to the selection rule reminiscent of formula (184) of the SI. Above θ_ω,all the peaks are present and the resulting spectrum is essentially classical.